Journal of Materials Chemistry C

ROYAL SOCIETY OF CHEMISTRY

PAPER

Cite this: *J. Mater. Chem. C*, 2020, **8**, 13798

The role of third cation doping on phase stability, carrier transport and carrier suppression in amorphous oxide semiconductors†

Austin Reed,[a] Chandon Stone,[a] Kwangdong Roh,[b] Han Wook Song,[c] Xingyu Wang,[d] Mingyuan Liu,[d] Dong-Kyun Ko,[e] Kwangsoo No[f] and Sunghwan Lee *[d]

Amorphous oxide semiconductors (AOSs), specifically those based on ternary cation systems such as Ga-, Si-, and Hf-doped InZnO, have emerged as promising material candidates for application in next-gen transparent electronic and optoelectronic devices. Third cation-doping is a common method used during the manufacturing of amorphous oxide thin film transistors (TFTs), primarily with the intention of suppressing carrier generation during the fabrication of the channel layer of a transistor. However, the incorporation of a third cation species has been observed to negatively affect the carrier transport properties of the thin film, as it may act as an additional scattering center and subsequently lower the carrier mobility from ~20–40 $cm^2 V^{-1} s^{-1}$ of In_2O_3 or a binary cation system (*i.e.*, InZnO) to ~1–10 $cm^2 V^{-1} s^{-1}$. This study investigates the structural, electrical, optoelectronic, and chemical properties of the ternary cation material system, InAlZnO (IAZO). The optimized carrier mobility (Hall Effect) of Al-doped InZnO is shown to remain as high as ~25–45 $cm^2 V^{-1} s^{-1}$. Furthermore, Al incorporation in InZnO proves to enhance the amorphous phase stability under thermal stresses when compared to baseline InZnO films. Thin film transistors integrating optimized IAZO as the channel layer are shown to demonstrate promisingly high field effect mobilities (~18–20 $cm^2 V^{-1} s^{-1}$), as well as excellent drain current saturation and high drain current on/off ratios ($>10^7$). The high mobility and improved amorphous phase stability suggest strong potential for IAZO incorporation in the next generation of high performance and sustainable optoelectronic devices such as transparent displays.

Received 3rd June 2020,
Accepted 10th September 2020

DOI: 10.1039/d0tc02655g

rsc.li/materials-c

Introduction

Transparent optoelectronic materials have gained significant attention for application in high performance devices such as next generation displays,[2,3] photovoltaics,[4] electrochromic devices,[5] and sensors.[6,7] Metal oxide-based semiconductors, specifically, are a promising group of transparent optoelectronic materials, now considered to be the vital building blocks for future device applications due to the unique combined properties of excellent optical transparency (from the visible to near-infrared regime) and high electrical conductivities.[8,9] Metal oxides have already seen wide implementation in various optoelectronic devices, depending on their electrical conductivity, as transparent electrodes by degenerately-doped oxides such as indium tin oxides (ITO)[10] and doped zinc oxides (ZnO),[11,12] as semiconducting active layers based on In_2O_3,[13] ZnO[14] or SnO_2,[15,16] and as insulators (*e.g.*, SiO_2, Al_2O_3, HfO_2) for dielectrics or encapsulation.[17,18]

The key pixel driving switches in display technologies, thin film transistors (TFTs), require a vast array of demanding material properties such as high carrier mobilities (usually defined as the "TFT field effect mobility"),[2,19] low thermal budgets during processing,[20] resilient phase stability,[21] and reliable device performance under high thermal and bias stress conditions.[22,23] Amorphous oxide semiconductors (AOSs), specifically those based on indium oxides, are receiving unique attention for TFT implementation due to their promisingly high carrier mobilities (>5–20 $cm^2 V^{-1} s^{-1}$ [13,22]) compared to conventional amorphous Si ones ($<\sim 1$ $cm^2 V^{-1} s^{-1}$),[2,24,25] low processing temperature requirements (ambient to 200 °C),[2,13] superior mechanical flexibility to their crystalline counterparts,[2]

[a] Department of Mechanical Engineering, Baylor University, Waco, TX 76798, USA
[b] Department of Electrical Engineering, Princeton University, Princeton, NJ 08544, USA
[c] Center for Mass and Related Quantities, Korea Research Institute of Standard and Science, Daejeon 34113, South Korea
[d] School of Engineering Technology, Purdue University, West Lafayette, IN 47907, USA. E-mail: sunghlee@purdue.edu
[e] Department of Electrical and Computer Engineering, New Jersey Institute of Technology, Newark, NJ 07102, USA
[f] Department of Materials Science and Engineering, KAIST, Daejeon 34141, South Korea

† Electronic supplementary information (ESI) available. See DOI: 10.1039/d0tc02655g

This journal is © The Royal Society of Chemistry 2020

and large area process-ability.[25] Indium oxide-based binary and ternary cation material systems show tremendous promise for use in next generation displays as these materials exceed the aforementioned material property and fabrication requirements. Unfortunately, undoped In_2O_3 experiences a rapid onset of microstructural crystallization at very low homologous temperatures ($T/T_m < 0.19$), *i.e.*, at 150 °C,[26,27] and struggles to maintain its amorphous phase structure. The inclusion of Zn in In_2O_3 has revealed a viable and promising binary cation material which specifically addresses the structural instability of undoped In_2O_3, Indium Zinc Oxide (IZO), as the addition of Zn into In_2O_3 proves to stabilize the temperature-sensitive amorphous phase of indium oxide. Furthermore, the reported carrier mobility of IZO has been shown to be as high as 20–40 $cm^2\ V^{-1}\ s^{-1}$ for Hall[20,28] and 15–30 $cm^2\ V^{-1}\ s^{-1}$ for TFT field effect mobilities.[3,19,29] Studies have dug deeper to further unveil the effects of the doping of In_2O_3-based materials, and the ternary cation system of indium gallium zinc oxides (IGZO) has proven to be even more popular than binary systems as the addition of Ga in IGZO allows for the controllable suppression of channel carrier density during TFT applications[2,30–32] (preferred for TFT devices where a low device off-state current is desired). In addition to Ga, more third cation species have been investigated as suitable material candidates such as Hf,[32,33] Si,[34] and Zr,[35] but the carrier mobilities (~3–10 $cm^2\ V^{-1}\ s^{-1}$[2,30,31]) are around 3–10 times lower than that of In_2O_3[20] or IZO.[20,28,29]

Therefore, securing strategies to develop a material system which both maintains a high carrier mobility (*e.g.*, $> \sim 20\ cm^2\ V^{-1}\ s^{-1}$) and suppresses carrier generation for TFT channel application is of significant importance and is necessary to expedite the realization of next-generation transparent displays which possess reliable performance, a fast switching speed, and, consequently, an ultra-high definition resolution. In this study, the ternary cation oxide system of indium aluminium zinc oxide (IAZO) is investigated with varying the Al concentration in IAZO thin films. The IAZO thin films were deposited using magnetron co-sputtering at room temperature. The structural, optical, and electrical properties were systematically characterized as a function of Al concentration and compared to those of baseline IZO samples. The carrier transport characteristics, as well as the dominant mechanisms for carrier density and resistivity and their relation to Al concentration, are discussed. Furthermore, amorphous IAZO-based TFTs were developed to objectively compare and validate device performance and parameters against IZO-based TFTs.

Experimental

Films of IZO and IAZO were deposited on cover slip glasses and Si wafers. The IZO films were sputter-deposited using a multi-target magnetron sputtering system from a commercially-available sintered IZO target (JX Nippon Mining & Metals USA, Inc.) at a DC power of 20 W in a pure Ar sputter gas atmosphere. IAZO films were prepared *via* co-sputtering of two source targets of IZO and Al under the same conditions for IZO and Al at RF powers of 10 W, 20 W, and 30 W to adjust the concentration of Al in the resulting IAZO films, leading to Al concentrations of 4 wt%, 8.9 wt%, and 16.7 wt%, determined *via* X-ray energy dispersive spectroscopy (EDS). The EDS elemental analysis is provided in Fig. S1 in the ESI.† Separate types of sputter power sources were intentionally selected for IZO (DC) and Al (RF) to limit the Al material concentration in the IAZO films as additional cation species (Al in this study) have been shown to act as scattering and/or trapping centers which deteriorate carrier transport and, consequently, overall electrical conductivity. Prior to film depositions, the chambers were pulled down to a base vacuum of $\sim 2 \times 10^{-7}$ Torr. Working pressures were maintained at a constant level of $\sim 4 \times 10^{-3}$ Torr. To create a uniform environment within the sputter chamber, ensure constant gas flow and pressure, and remove any residual contaminants on the surface of the targets, a 300 second pre-sputter coat was used prior to each deposition. All depositions were performed at room temperature.

The electrical properties of the series of IAZO films were characterized through custom-built four-point probe apparatus and a Hall Effect electromagnetic system; carrier densities and mobilities were determined *via* Hall Effect measurements at a current source of <1 nA and a magnetic field magnitude of 5200 Gauss from a GMW Associates electromagnet. The source current and specimen voltages were monitored with a Keithley 4200-SCS unit with an input impedance greater than 1 TΩ. To complement the measurements taken using the four-point probe and ensure accuracy, resistivity values were also determined *via* Hall measurements.

The amorphous and crystalline structures of the IAZO films were characterized *via* X-ray diffraction (XRD) analysis utilizing a Siemens D5000 diffractometer with Cu K-α radiation (λ = 1.54 Å) at an operating voltage of 40 kV and an amperage of 40 mA. Glancing incident angle diffraction measurements with an incident angle of approximately 1° were taken to maximize the X-ray penetrating depth in the films and hence to obtain a reasonably high diffraction intensity for the IAZO thin film analysis. The surface topographic microstructural images and root mean square (RMS) roughness of IAZO were obtained using atomic force microscopy (AFM, Veeco Multimode with Nanoscope V) in the tapping mode with a Bruker Si cantilever (a tip frequency of 330 kHz). A scanning electron microscope (SEM, FEI Quanta 200 FEG SEM) was used to complement AFM surface investigations. Energy dispersive X-ray spectroscopy (EDS, Oxford Instruments X-Max80) coupled to SEM was used to quantify the elemental composition of the prepared films. The optical properties were measured using a Varian Cary 50 UV-Vis spectrometer in the visible regime wavelength range of 300–800 nm. An FS-1 multi-wavelength ellipsometer (Film Sense) with an incident and detection angle of 65° was used to measure the film thickness.

To provide proof of concept *via* device application, bottom-gated amorphous oxide TFTs were fabricated utilizing IAZO as the functioning channel layer material (30 nm). For a valid baseline comparison during the TFT performance analysis, IZO-channel TFTs were developed utilizing identical sputtering parameters. The channel layers of both sets of TFTs (IZO and IAZO)

were deposited using the aforementioned sputtering parameters, with the exception of substituting the sputter gas with an ultra-high purity blend of Ar/O_2 (80/20 vol. ratio) to limit excess carrier generation *via* the formation of oxygen vacancies. Heavily doped Si wafers (0.003–0.005 Ω cm) were used as the bottom gate layer, with thermally grown SiO_2 (50 nm) serving as the gate dielectric material. Source and drain (S/D) terminals (100 nm) were grown *via* DC sputtering of Ti (40 W) with pure Ar sputter gas. Channel and S/D patterns were defined using an *in situ* shadow masking technique. Device performances were evaluated with an Agilent 4155B semiconductor parameter analyzer in a light-tight probe station under ambient conditions. More than 18 TFT devices were fabricated for both sets of TFTs (IZO and IAZO) to gather reliable data and provide evidence of repeatability.

Results and discussion

Microstructure and elemental distributions

A schematic diagram of the co-sputtering process is provided in Fig. 1(a), where two sputter guns, out of a total of three, for a multi-target sputtering system are shown, and samples are delivered from a load lock chamber to the main chamber to maintain consistent low chamber vacuum conditions by minimizing particle impurities introduced by exposure to ambient air. Fig. 1(b) shows the RMS roughness of the IAZO films as a function of Al concentration in weight% (Al wt%, samples denoted as # wt% IAZO), along with the associated AFM topographic images (right). The AFM images and roughness values were measured for all 70 nm-thick IAZO films over the area of 1 μm × 1 μm. The RMS roughness increases with increasing Al concentration: the roughness is found to be 1.43 nm for 0 wt% IAZO (*i.e.*, IZO), 2.70 nm for 4 wt% IAZO, 3.30 nm for 8.9 wt% IAZO, and 4.86 nm for 16.7 wt% IAZO. The increasing roughness is attributed to the distortion and increased disorders in the material due to the increasing incorporation of additional species (*i.e.*, Al).

Plan-view SEM micrographs shown in Fig. 2(a) complement the AFM investigations and support the RMS roughness shown in Fig. 1(b). For 0 wt% IAZO, a very smooth surface with no specific microfeatures is seen; yet, with increasing Al concentration, as first observed in the AFM imaging, a clear evolution of film microstructures is depicted. Note that, while the microstructures show grain-like features in the Al-incorporated films, the features are due to the surface morphological information as no evidence on the amorphous/crystalline structure is provided by the SEM micrographs. To further investigate the structural properties of the IAZO films, particularly for the features presented in the higher Al concentration films, X-ray diffraction measurements were made and will be discussed in detail with Fig. 3. EDS elemental distribution analyses were performed to investigate the elemental distribution of the IAZO films, particularly to see if any elemental segregation is responsible for the microstructural changes observed in Al-doped films. EDS mapping images for 8.9 wt% IAZO and 16.7 wt% IAZO are presented in Fig. 2(b) and (c), respectively, where all the elements of In, Al, Zn and O are confirmed to be uniformly distributed in the films without any elemental segregation or separation.

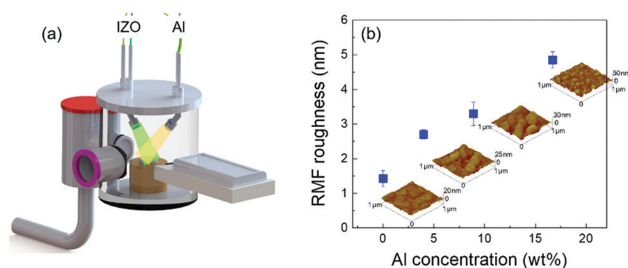

Fig. 1 (a) Schematic of co-sputtering from sintered ceramic IZO and Al metal targets where the IZO target is connected to a DC sputter gun and the Al target is loaded to a RF gun, which is strategically designed to limit the deposition rate of Al and its concentration in the resulting IAZO film; (b) RMS surface roughness as a function of Al concentration in wt%, where the roughness increases with increasing Al concentration. Inset: AFM images obtained over the area of 1 μm × 1 μm shown with Al concentration, from which the RMS roughness was determined.

Amorphous/crystalline structure through GIAXRD: as-deposited

Fig. 3 presents the glancing incident angle XRD (GIAXRD) spectra of the as-deposited IAZO films as a function of Al content including IZO as 0 wt% IAZO. It should be noted that no crystalline features are observed in all the series of IAZO films in the as-deposited diffraction patterns, which indicates that all the resulting films are in the amorphous state. The observed amorphous diffraction curves with no metal Al features also confirm the complete incorporation of sputtered Al into the resulting IAZO films during the reactive co-sputtering. The as-deposited XRD patterns of IAZO will be compared later with those of the annealed IAZO films and will be related with the effect of Al incorporation on the amorphous phase stability. In a series of XRD patterns, a broad amorphous peak appearing in the diffraction range of $15^\circ < 2\theta < 35^\circ$ is seen, which can be attributed to glass substrates.

Evaluation of electrical properties as a function of Al concentration

The electrical properties of IAZO measured using the Hall Effect system and the four-point probe are displayed in Fig. 4. The resistivity shown in Fig. 4(a) increases with increasing Al concentration in IAZO: the lowest resistivity of 4.1×10^{-4} Ω cm is achieved from 0 wt% IAZO (*i.e.*, IZO), then the resistivity monotonically increases as the Al concentration increases, and the highest resistivity of ∼3.8 Ω cm is obtained at the highest Al concentration (16.7 wt%) in this study. The overall resistivity is a combined result of carrier density (n) and carrier mobility (μ) according to the typical resistivity equation, $\rho = 1/\sigma = 1/qn\mu$. The carrier density and carrier mobility are presented in Fig. 4(b) and (c), respectively. As the incorporation of Al increases in the IAZO films, the carrier density decreases from 4.7×10^{20} cm^{-3} (0 wt% Al) to $\sim 7.9 \times 10^{17}$ cm^{-3} (16.7 wt% Al). This carrier density trend can be attributed to the following two

 This journal is © The Royal Society of Chemistry 2020

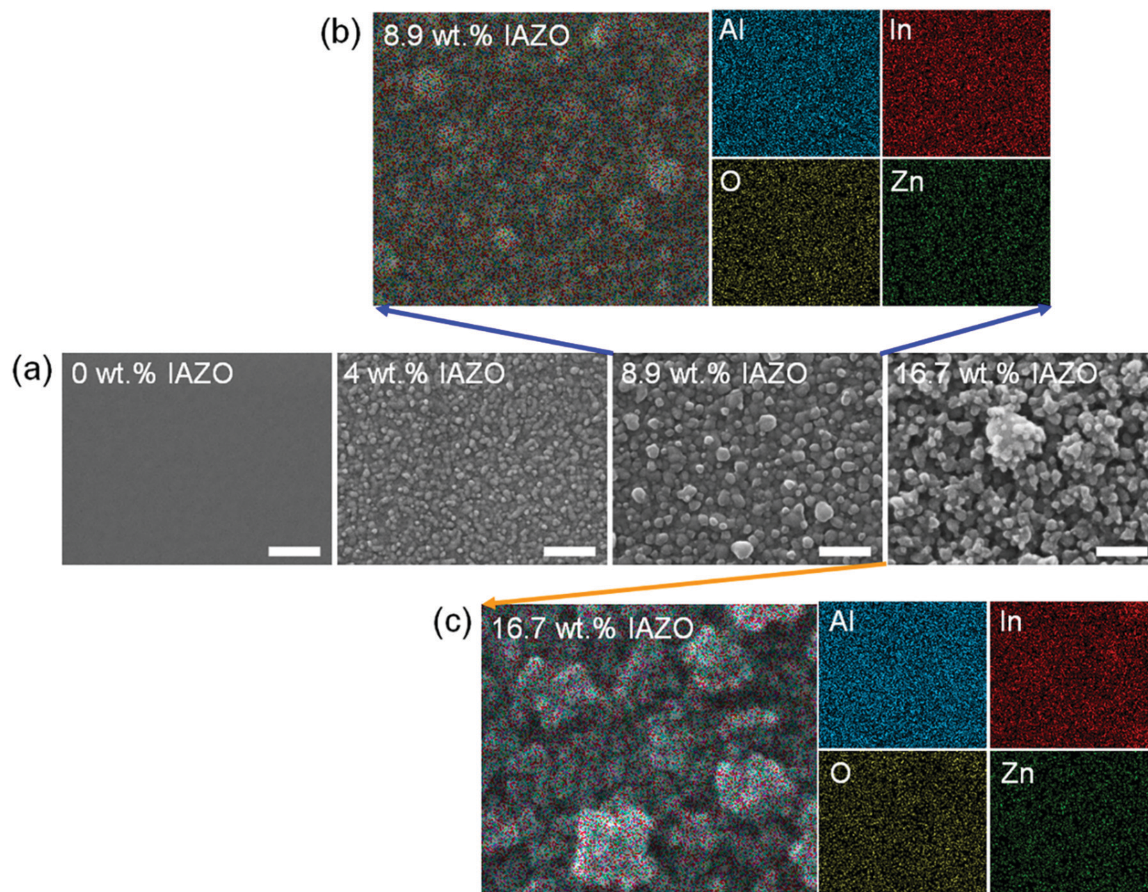

Fig. 2 (a) Plan-view SEM micrographs as a function of Al concentration where 0 wt% IAZO presents a very smooth surface; however, the microstructural evolution is clearly observed with Al concentration. EDS elemental mapping analysis of (b) 8.9 wt% IAZO and (c) 16.7 wt% IAZO films, from which it is confirmed that all element species of Al, In, O and Zn are uniformly distributed across the measured sample area with no significant elemental segregation or separation.

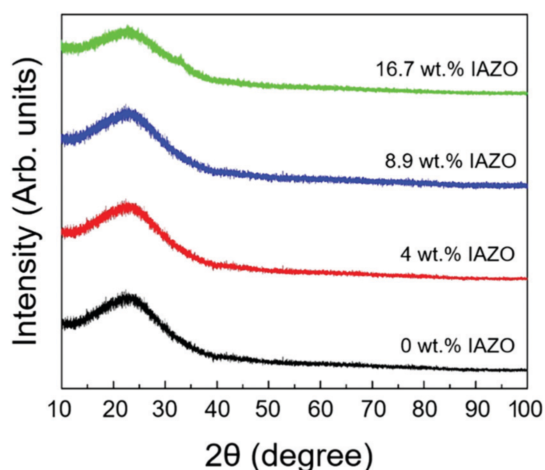

Fig. 3 As-processed XRD spectra of a series of IAZO films as a function of Al concentration where no significant crystalline diffractions are detected, indicating that all IAZO films are in the amorphous state.

reasons: first, as reported, Zn is not activated to contribute to the generation of free carriers in IZO, and the carrier density is mainly attributed to non-stoichiometric oxygen in indium oxides.[36] With increasing Al concentration in IAZO, the stoichiometric conditions of oxygen change since the incorporated Al preferentially reacts with oxygen rather than existing as metallic Al or metallic compounds, which is supported by our XRD analysis showing the absence of crystalline features in Fig. 3. This claim is also supported by the fact that the binding (or dissociation) energy between Al and O (Al–O bonding, 5.32 eV) is greater than those for In–O and Zn–O bondings of 3.74 and 2.95 eV, respectively.[37–40] The presence of high metal-oxygen binding energy components is known to suppress the carrier generation in indium oxide-based AOS materials since the number of overall oxygen vacancies reduces.[41–43] Second, with an increase in Al incorporation, the number of In–O bondings per unit volume decreases, which has been studied previously to determine the carrier density of AOS materials.[41–43] This may account for the reduction in carrier density with increasing Al incorporation into IAZO films.

The carrier mobility as a function of Al concentration is shown in Fig. 4(c). The IZO (0 wt% IAZO) shows a carrier mobility of $\sim$31.8 $cm^2\ V^{-1}\ s^{-1}$ and a maximum mobility of $\sim$34.7 $cm^2\ V^{-1}\ s^{-1}$ is reached at an Al concentration of 4 wt%. At a higher concentration of Al, the carrier mobility steeply

This journal is © The Royal Society of Chemistry 2020

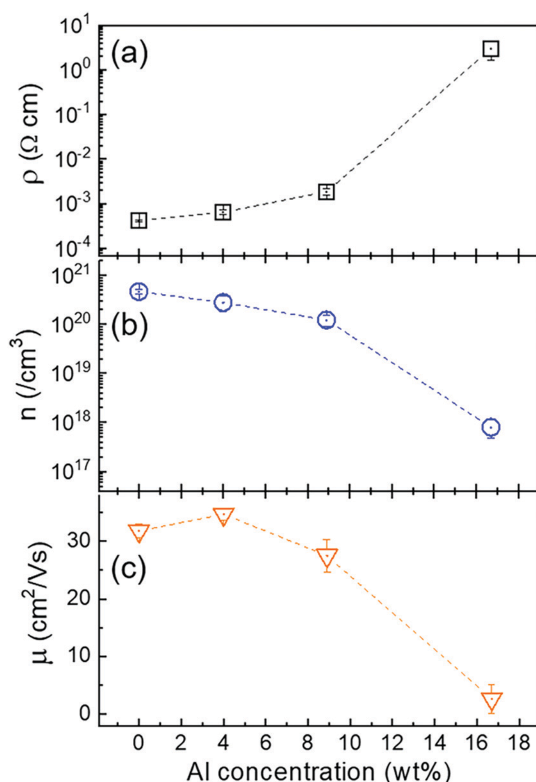

Fig. 4 Electrical properties of the IAZO films as a function of Al concentration: (a) resistivity, (b) carrier density and (c) carrier mobility where the suppression of carrier generation and the scattering effect are evidently observed.

decreases with increasing Al: at Al concentrations of 8.9 and 16.7 wt%, the mobilities are ~27.5 and 2.6 $cm^2\ V^{-1}\ s^{-1}$, respectively. Although carrier transport in a multi-cation system is complicated, there are three known primary mechanisms that govern the transport in the IAZO system. The first is the ionized (or charged) impurity scattering. It has been theoretically[44–46] and experimentally[1,47,48] studied that oxygen vacancy is the primary intrinsic dopant in AOS to generate free carriers. This oxygen vacancy mechanism creates two free electrons per oxygen vacancy, following the defect equation given below:

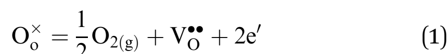

$$O_O^{\times} = \frac{1}{2}O_{2(g)} + V_O^{\bullet\bullet} + 2e' \quad (1)$$

where $V_O^{\bullet\bullet}$ is the oxygen vacancy and e' is the electron. In general, indium oxide-based materials that are prepared under reducing conditions are degenerate semiconductors with a high carrier concentration and thus have a high density of oxygen vacancies. In this high carrier concentration regime (typically $> 10^{20}\ cm^{-3}$ in AOSs), ionized impurity scattering from the large number of charged oxygen vacancies dominates the carrier transport. With an increase in carrier concentration, an enhancement in ionized impurity scattering reduces the carrier mobility.

The second mechanism is the neutral (non-charged) scattering which arises from the atomic disorder[49,50] caused by Al incorporation. Similar carrier transport behavior (*i.e.*, reduction in carrier mobility) due to the addition of third elements has been observed in IGZO[51,52] as well as other ternary cation systems including IHfZO (*i.e.*, Hf as the third element),[32,33,53] ISiZO (*i.e.*, Si as the third element)[34] and IZrZO (*i.e.*, Zr as the third element).[35] In general, the carrier mobility of those ternary cation AOS materials (3–10 $cm^2\ V^{-1}\ s^{-1}$)[33,34] is much lower than that of their binary counterparts (*e.g.*, IZO) of 20–40 $cm^2\ V^{-1}\ s^{-1}$.[20,29]

The third is the effect of charge screening. When the carrier concentration falls below the degenerate regime, negatively charged electrons, which are the majority carriers in our material, screen positively charged oxygen vacancies (doubly-charged as shown in the defect equation (eqn (1)) above) due to the Coulomb potential, by which carrier electrons are localized around the oxygen vacancies.[54] Therefore, the screening mechanism facilitates the transport of other free carriers that are not involved in the charge screening. Hence, in this low carrier concentration regime, the carrier mobility increases with increasing carrier density. The carrier mobility trend shown in Fig. 4(c) can be understood based on these three mechanisms. The initial increase in carrier mobility, from 31.4 $cm^2\ V^{-1}\ s^{-1}$ at 0 wt% IAZO to 35.1 $cm^2\ V^{-1}\ s^{-1}$ at 4 wt% IAZO Al, is attributed to the ionized impurity scattering mechanisms (*i.e.*, a higher carrier density leads to a lower carrier mobility in this regime). Then, the carrier mobility decreases with increasing Al concentration, which is due to the combined effect of neutral scattering (*i.e.*, an increase in Al concentration increases the atomic disorder) and the limited charge screening (*i.e.*, a higher carrier density leads to a higher carrier mobility).

Carrier scattering mechanisms

The carrier transport behavior is further detailed by plotting carrier mobility *vs.* carrier density, as presented in Fig. 5. To provide a general trend of carrier mobility as a function of carrier density, additional sets of IAZO films were developed at various volume ratios of the Ar/O_2 sputter gas. Additionally, the values from our previous report[1] for 0 wt% IAZO (*i.e.*, IZO) are also included in this plot to provide a broader range of carrier density for 0 wt% IAZO. It should be noted that the overall mobility of 0 wt% IAZO is higher than that of Al-incorporated films. In particular, 16.7 wt% IAZO exhibits a significantly low carrier mobility of ~2.6 $cm^2\ V^{-1}\ s^{-1}$. In Fig. 5, the maximum mobility of each IAZO film decreases with increasing Al concentration and the maximum mobility is obtained at a lower carrier concentration compared to that of 0 wt% IAZO (*e.g.*, max ~ 50 $cm^2\ V^{-1}\ s^{-1}$ for 0 wt%. IAZO at $1.5 \times 10^{20}\ cm^{-3}$ *vs.* max ~ 38 $cm^2\ V^{-1}\ s^{-1}$ for 8.9 wt% IAZO at $1 \times 10^{19}\ cm^{-3}$). This decrease in carrier mobility with increasing Al concentration results from the increased scattering events by Al (*i.e.*, neutral scattering) causing further distortion of short range orders.[49,50,55] A transition in the carrier transport behaviors from charge screening to ionized impurity scattering can be clearly seen in Fig. 5. In the lower carrier density regime, for example carrier density $< \sim 10^{20}\ cm^{-3}$ for 0 wt% and 4 wt% IAZOs, the carrier mobility increases with increasing carrier density, which is due to the charge screening effect. However, in the higher carrier

This journal is © The Royal Society of Chemistry 2020

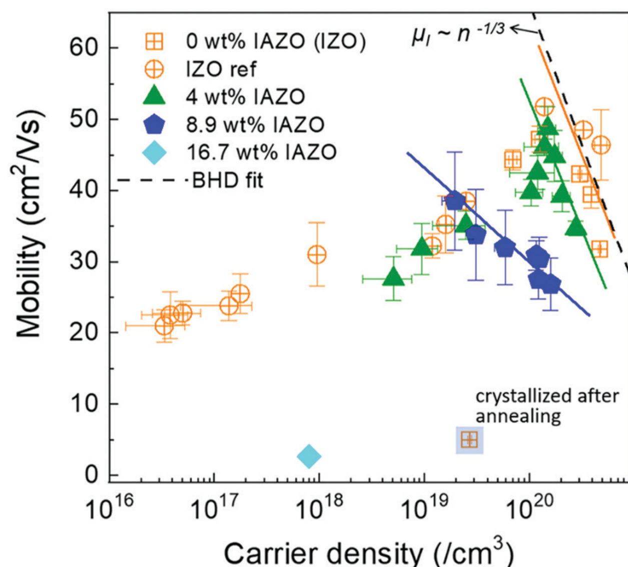

Fig. 5 Plot of mobility *vs.* carrier density where changes in scattering mechanisms as a function of carrier density and Al concentration are identified: ionized impurity scattering is in dominant charge of carrier transport for 0 and 4 wt% IAZO; however, further incorporation of Al deviates the carrier transport from the ionized impurity scattering mechanism and other mechanisms such as neutral scattering become more dominant. In the lower carrier density regime $< \sim 10^{19}$ cm^{-3}, the carrier transport is governed by charge screening, depending on the Coulomb potential between negative charges (*i.e.*, electrons) and positive charges (*i.e.*, mostly oxygen vacancies). Note the additional data sets of IAZO prepared at various Ar/O_2 sputter gas ratios and from our previous report.[1]

density regime, for example carrier density $> 10^{20}$ cm^{-3} for 0 wt% and 4 wt% IAZOs, the carrier mobility decreases with further increasing the carrier density, which is attributed to the ionized impurity scattering.

The theoretical mobility that is governed by the ionized impurity scattering mechanism can be estimated using the Brooks–Herring–Dingle (BHD) model:[56]

$$\mu_{\mathrm{I}} = \frac{24\pi^3(\varepsilon_0\varepsilon_{\mathrm{r}})^2\hbar^3 n}{e^3(m^*)^2 g(x) Z^2 n_{\mathrm{I}}} \quad (2)$$

where μ_{I} is the mobility that is governed by the ionized impurity scattering mechanism, and Z and n_{I} are the charge and density of the ionized scattering centers, respectively. In this study, $Z = 2$ since doubly charged oxygen vacancies work as ionized impurities and a density ratio of charge carrier/scatter center $n/n_{\mathrm{I}} = 2$ is used according to the defect equation (eqn (1)). The scattering function $g(x)$ is defined as

$$g(x) = \ln\left(1 + \frac{4}{x}\right) - \frac{1}{\left(1 + \frac{x}{4}\right)} \quad (3)$$

and

$$x = \frac{e^2(m^*)}{\pi\varepsilon_0\varepsilon_{\mathrm{r}}\hbar^2\sqrt[3]{3\pi^5 n}} \quad (4)$$

where ε_0 and ε_{r} denote the absolute and relative dielectric constants, respectively, and m^* is the effective mass of the free carriers (*i.e.*, electrons). For these calculations for IAZO, the values of $m^* = 0.3m_{\mathrm{e}}$ and $\varepsilon_{\mathrm{r}} = 9$, which are typically selected for indium oxide-based semiconductors such as ITO, IZO and IGZO, were taken from the literature.[49,57,58] The μ_{I} value calculated from the BHD theory, due to the carrier scattering events from ionized oxygen vacancies, is plotted as a function of carrier density in Fig. 5 with a dashed line. This plot shows the relationship of the mobility of ionized impurities with carrier density, $\mu_{\mathrm{I}} \sim n^{-1/3}$, according to eqn (2)–(4).[56] Note that (i) the experimentally measured carrier mobility using Hall Effect is similar to the calculated μ_{I} for 0 wt% IAZO (*i.e.*, IZO) with a slight deviation due possibly to the selected values (m^* and ε_{r}) for the calculation or other minor scattering events, and (ii) the carrier mobility of 4 wt% IAZO still shows a similar trend with carrier density of $\mu_{\mathrm{I}} \sim n^{-1/3}$, indicating that the carrier transport mechanism for 4 wt% IAZO still dominantly follows the ionized impurity scattering mechanism. However, the further incorporation of Al considerably deviates the measured mobility from the BHD model and its trend, which implies that other scattering mechanisms become dominant with increasing Al impurity concentration, which is in agreement with the discussion regarding possible scattering mechanisms due to the Al incorporation. For the lower carrier density regime $< \sim 10^{19}$ cm^{-3}, the carrier mobility increases with increasing carrier density, which is due to the enhanced screening effect with increasing carrier density (or reduced charge carrier localization due to the decreased Coulomb potential) before the ionized impurity scattering mechanism becomes dominant at a carrier density higher than $\sim 10^{20}$ cm^{-3}.

Optoelectronic properties: UV-Vis and bandgap analyses

The visible-regime optoelectronic characteristics of IAZO films are presented in Fig. 6, for which the UV-Vis measurements were made on a series of IAZO films on slide glasses and a baseline scan was performed on a bare slide glass substrate to exclude the substrate effect from each result. As a figure of merit, all the UV-Vis measurements were carried out for a film thickness of approximately 70 nm. Fig. 6(a) shows the optical transmittance of the films as a function of Al concentration in the visible regime wavelength range of 300 to 800 nm. High transmittance values over 85% in the visible regime and 90% at a wavelength of 500 nm were obtained for 0 wt% and 4 wt% IAZO films and then decreased to 86% for 8.9 wt% IAZO and 41% for 16.7 wt% IAZO films. The decrease in the visible-regime transmittance with increasing Al concentration is ascribed to increased absorption and scattering due to Al incorporation. A clear red-shift of the UV absorption edge can be seen in Fig. 6(a) with increasing Al concentration. In order to determine the optical bandgap of the IAZO films, Tauc plots of $(\alpha h\nu)^2$ *vs.* $h\nu$ for the direct bandgap transition (a single electron plus a single photon) of IAZO films[55] are shown as a function of Al concentration in Fig. 6(b), where α is the absorption coefficient and $h\nu$ is the light energy with the Planck constant h and the frequency ν.[55,59] Although the Tauc theory is more intended to interpret crystalline semiconductors, the addition of perturbations to the crystalline lattice allows for the analysis

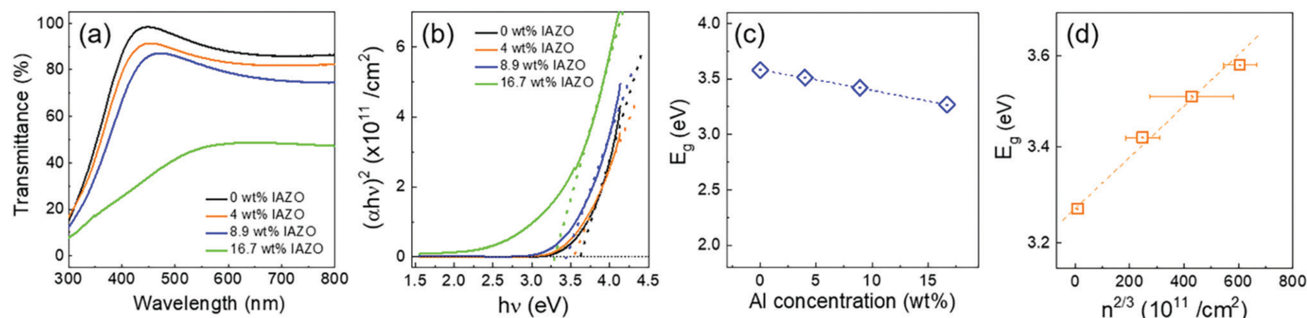

Fig. 6 (a) UV-Vis spectroscopy measurements of (a) transmittance in the visible regime where IAZO with Al concentration lower than 10 wt% shows good optical transparency over 80%; (b) Tauc plots of $(\alpha h\nu)^2$ *vs.* $h\nu$ as a function of Al concentration in the IAZO films; (c) the trend of optical bandgap, E_g, that is extracted from the Tauc plots in (b); and (d) a plot of E_g *vs.* $n^{2/3}$ with a linear relationship, indicating the E_g shrinkage shown in (c) relevant to the Burstein–Moss effect.

of bandgap for amorphous solids to a limited extent due to the lack of long-range order in amorphous semiconductors.[55,59] Therefore, Tauc plots are only to be used to determine the onset of interband transition by extrapolating a linear portion line to the zero absorption (*i.e.*, *x*-axis) without details about the types of interband transition.[55,59] Since crystalline In_2O_3 is known to have direct bandgap transition, the Tauc plots in Fig. 6(b) were constructed by $(\alpha h\nu)^2$ *vs.* $h\nu$. Fig. 6(c) summarizes the change in the optical bandgap of the IAZO films with increasing Al concentration. The optical bandgaps ($E_{g,op}$) of the IAZO films are found to be ~3.63, 3.51, 3.42 and 3.27 eV for 0, 4, 8.9 and 16.7 wt% IAZO films, respectively, which present a consistent decrease in bandgap. All the IAZO films show similar optical bandgaps of In_2O_3-based semiconductors: 3.5–3.9 eV for In_2O_3,[60–62] 3.6–4.2 eV for ITO,[60,62–64] 3.1–3.9 eV for IZO[64–66] and 3.1–3.7 eV for IGZO,[67,68] which further confirms that Al in the matrix is well incorporated without significant metallic Al or segregation. The linear relationship between $E_{g,op}$ and $n^{2/3}$, plotted in Fig. 6(d), indicates that the bandgap shrinkage observed in Fig. 6(c) with increasing Al concentration can be understood by the Burstein–Moss (BM) theory that relates the carrier density (n) and the change in bandgap in response to photo-excitation:[67,69]

$$\Delta E_G = \left(\frac{h^2}{8m^*}\right)\left(\frac{3n}{\pi}\right)^{2/3} \quad (5)$$

where m^* is the effective mass and h is the Planck constant.

Phase stability in response to thermal stress

In order to investigate the thermal stability of IAZO films as a function of Al concentration, the films were annealed in air at 500 °C and their amorphous/crystalline structures were characterized using GIAXRD as for the as-deposited patterns shown in Fig. 3. The XRD spectra of the samples annealed at 500 °C are presented in Fig. 7. It should be noted that the incorporation of Al into the IZO matrix significantly enhances the amorphous phase stability. Although undoped In_2O_3 or indium tin oxide in the amorphous state crystallizes rapidly at temperatures as low as 125–150 °C,[26,27] the amorphous phase stability of In_2O_3-based oxide semiconductors such as IZO and IGZO is enhanced

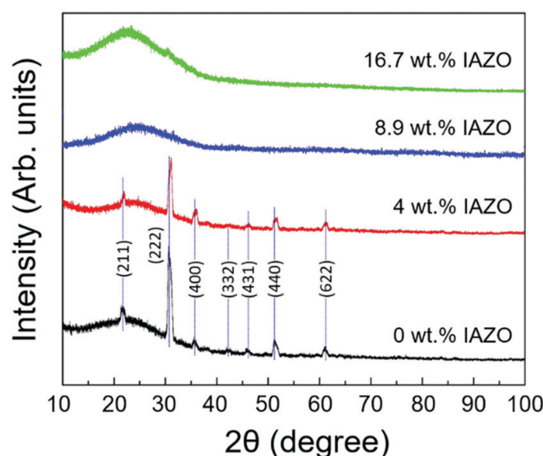

Fig. 7 XRD spectra obtained from annealed IAZO films as a function of Al concentration: as previously reported, 0 wt% IAZO (*i.e.*, IZO) crystallizes after annealing at 500 °C for an hour and the addition of Al clearly slows the crystallization kinetics and stabilizes the amorphous phase, which is confirmed by the fact that no significant crystalline diffraction peaks are observed in 8.9 wt% and 16.7 wt% IAZO films.

by the addition of ZnO that slows the crystallization kinetics.[27,70,71] It has been widely believed that the limited solubility of divalent tetrahedrally bonded Zn–O in the octahedral In–O bixbyite structure gives rise to the enhanced amorphous stability.[27,70,71] The amorphous state remains up to a temperature of approximately 500 °C, at which amorphous IZO or IGZO transforms to the poly-crystalline structure in an hour.[36,72] Similar results were achieved after annealing at 500 °C as shown in the bottom curve for 0 wt% IAZO (*i.e.*, IZO) in Fig. 7 with the characteristic In_2O_3 bixbyite peaks strongly from the (222) plane at a diffraction angle, 2θ, of approximately 30.8° and other planes including (211), (400), (332), (431), (440) and (622) planes at 2θ values of 21.5°, 35.7°, 41.9°, 45.6°, 51.3° and 60.7°, respectively (JCPDS # 00-006-0416). Note that it is clearly observed that the crystalline features become weaker with increasing Al concentration. The XRD spectrum of 4 wt% IAZO exhibits slight shifts of the diffraction peaks to higher diffraction angles, which is likely to be attributed to lattice

 This journal is © The Royal Society of Chemistry 2020

distortion and increased structural disorders due to the addition of Al into the matrix. For 8.9 wt% and 16.7 wt% IAZO, only a minor amorphous hump is observed at $2\theta = \sim 32$–33° and no crystalline evidence was found. In the case of IAZO, the additional cation species of Al further frustrates the lattice to be accommodated into the cubic bixbyite crystal structure and require a higher activation energy for an ordering transformation (*i.e.*, crystallization) to occur.[55]

This enhanced phase stability is of significant importance in TFT channel applications since a change in amorphous/crystalline states may cause unfavorable device performance instabilities during operation. Therefore, the enhanced thermal stability may further contribute to prolonging the TFT lifetime with consistent performance.

Comparison of electrical properties between IZO and IAZO with annealing temperature

In order to investigate the behaviors of the IAZO electrical properties due to annealing, changes in resistivity, carrier density and carrier mobility were characterized through Hall Effect measurements as a function of annealing temperature. For the measurements, 8.9 wt% IAZO films were selected since: (i) this study with IAZO aims to contribute to transparent electronic and optoelectronic applications that require both electrical conductivity and optical transparency in the visible regime. The visible regime transmittance of 16.7 wt% IAZO is found to be considerably inferior to other Al concentration IAZO films; (ii) for TFT channel application, it has been challenging to suppress the carrier density in undoped In_2O_3 and binary cation system of IZO, which is required to limit the off-state current as low as possible and also to achieve high conductance that is defined as the ratio of change in drain current over change in gate bias, $g = dI_D/dV_G$.[73] The 4 wt%. IAZO shows no significant carrier suppression effect; and (iii) the phase stability should also be considered to ensure the reliable and stable device performance for sustainable operations. Although it is clearly shown that the Al incorporation leads to an enhancement in amorphous phase stability, the 4 wt% IAZO film still crystallizes, seen by the series of diffraction peaks after annealing at 500 °C presented in the XRD pattern in Fig. 7, which may cause performance instability for the material and potential devices during operations. With these rationales, the 8.9 wt% IAZO that demonstrated high mobility, excellent visible-regime transmittance, and enhanced phase stability was selected for further investigations for the electrical properties for potential TFT device implementation.

As a figure of merit, the 8.9 wt% IAZO electrical properties are then compared to those of 0 wt% IAZO (*i.e.*, IZO) as a function of annealing temperature in Fig. 8. The initial resistivity of the 8.9 wt% IAZO film (1.84×10^{-3} Ω cm) is higher than the IZO resistivity (4.18×10^{-4} Ω cm) since the third cation species of Al is expected to limit the generation of charge carriers and increase scattering events in IAZO, which is evidenced in the plots of carrier density and carrier mobility in Fig. 8(b) and (c), respectively. Up to an annealing temperature of 200 °C, no significant changes are observed in the resistivity for IZO as a slight decrease in carrier density is compensated by an increase in carrier mobility for IZO. However, the resistivity of 8.9 wt% IAZO displays a slight decrease from 1.64×10^{-3} Ω cm to 1.45×10^{-3} Ω cm when annealed at the same temperature, during which the carrier density at the regime $>10^{20}$ cm^{-3} increases from $\sim 1.25 \times 10^{20}$ cm^{-3} to $\sim 1.61 \times 10^{20}$ cm^{-3} and the carrier mobility decreases from 30.4 cm^2 V^{-1} s^{-1} to 26.8 cm^2 V^{-1} s^{-1}. This shift can be understood by the ionized impurity scattering mechanism, where the slight increase in carrier density leads to more scattering events and, therefore, a decrease in the carrier mobility of 8.9 wt% IAZO. The resistivity for both samples starts to increase as annealing temperature further increases until 400 °C, which is attributed to a reduction in carrier density since the mobility values for both cases are slightly higher than those at lower annealing temperatures. It should be noted that at a temperature of 500 °C, the IZO resistivity steeply increases to 4.62×10^{-2} Ω cm, which is higher than 5.96×10^{-3} Ω cm of IAZO, which is due to the approximately 10-fold lower mobility of IZO (4.8 cm^2 V^{-1} s^{-1}) than IAZO (33.8 cm^2 V^{-1} s^{-1}) while the carrier density of IZO (2.71×10^{19} cm^{-3}) is similar. At 500 °C, the observed difference in carrier mobility mainly accounts for the phase transformation of amorphous IZO to the polycrystalline state where the carrier transport is dominantly limited by the grain-boundary scattering mechanism[74,75] while no

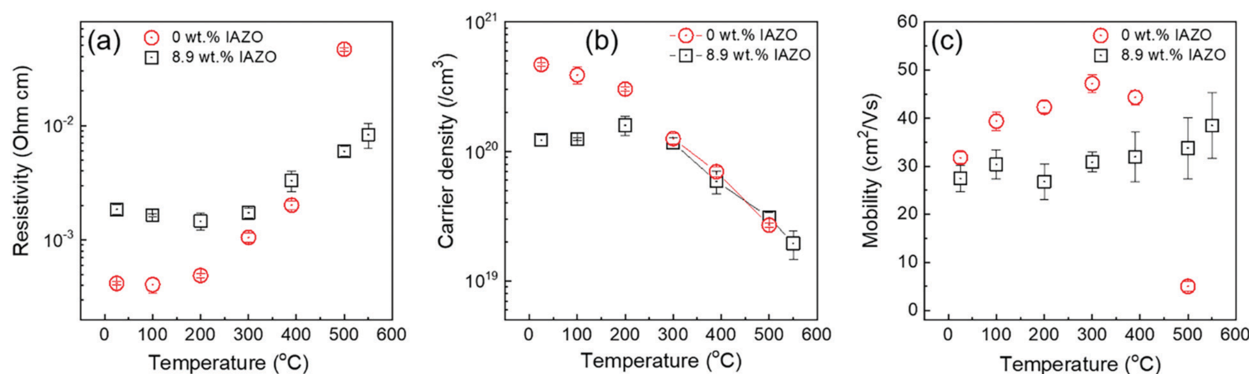

Fig. 8 (a) Electrical properties of 0 wt% IAZO (*i.e.*, IZO) and 8.9 wt% IAZO as a function of annealing temperature: (a) resistivity, (b) carrier density and (c) carrier mobility.

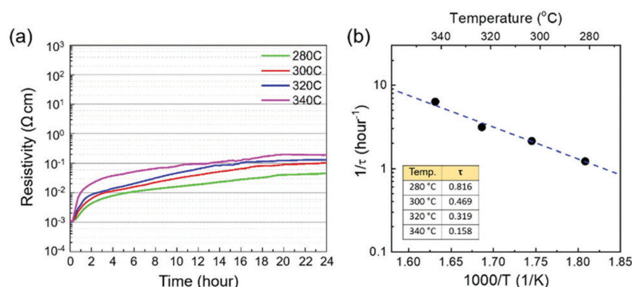

Fig. 9 (a) *In situ* resistivity measurements as a function of time and measurement temperature where the rate of change in resistivity at all the measured temperatures is fast for the first two hours of the measurement and then it decreases; (b) Arrhenius plot of $1/\tau$ *vs.* reciprocal temperature, which shows that the rate of resistivity change of IAZO is a thermally activated process with an activation energy of 0.79 eV.

significant degradation in mobility is found in IAZO. The high carrier mobility maintained after relatively high-temperature annealing and the enhanced amorphous stability of IAZO may be of significant importance for sustainable and reliable device performance when the material is incorporated in electronic and optoelectronic devices such as TFTs and solar cells. Note that the carrier density is similar to each other for the two IAZO specimens (0 wt% and 8.9 wt% Al concentration) at annealing temperatures greater than 300 °C in this study, which may be attributed to the fact that carrier annihilation (or generation) is more sensitive to temperature at higher temperatures and the effect of Al incorporation becomes weaker for carrier activation. In order to further investigate the dominant conduction mechanism in IAZO, *in situ* resistivity measurements were made and the results are discussed with Fig. 9.

In situ resistivity measurements and activation energy for resistivity

The resistivity of 8.9 wt% IAZO was measured *in situ* using a typical four-contact setup for longer than 24 hours as a function of measurement temperature from 280 °C to 340 °C in a 20 °C step. The resistivity results are presented in a resistivity *vs.* time plot, as shown in Fig. 9(a). The initial resistivity in all measurements is similar ($\sim 1 \times 10^{-3}$ Ω cm) since the samples were simultaneously prepared at the same sputter run. It should be noted that (i) the rate of change in resistivity is thermally activated; (ii) the resistivity increases fast during the first two hours and then the rate of resistivity change decreases, reaching a resistivity plateau (*i.e.*, (pseudo)equilibrium state); and (iii) among the curves as a function of temperature, it is clearly observed that the higher temperature leads to the faster rate of change in resistivity due to enhanced reaction kinetics at higher temperatures. A time constant (τ) is determined when the initial resistivity (ρ_0) becomes as high as $2\rho_0$ for each temperature. Then, the inverse of the time constant ($1/\tau$) provides a rate of the reaction for the resistivity change. In Fig. 9(b), a set of $1/\tau$ is plotted on a conventional Arrhenius plot of $1/\tau$ *vs.* inverse absolute temperature ($1/K$). From the Arrhenius plot, the activation energy for the rate of resistivity change in IAZO is determined to be ~0.79 eV, which is slightly lower than E_a ~ 1.06 eV of amorphous IZO (or 0 wt% IAZO) reported in our previous study[21] wherein a lower E_a means that the resistivity scales less with temperature, which is supported by the results shown in Fig. 8(a).

TFT devices integrating the IAZO channel and the performance

To investigate the potential use of IAZO as a channel layer material in AOS TFTs, test devices with IAZO channel layers (30 nm) were fabricated in a gate-down configuration on top of thermally grown SiO_2 (50 nm)/Si (heavily doped p-type) substrates. For accurate baseline comparisons, TFTs with IZO channels (30 nm) were developed to act as a point of reference for analyzing the performance of IAZO-based TFTs. Both the output and transfer characteristics of the reference IZO-based devices can be observed in Fig. 10(a) and (b), respectively, which align with previous reports on amorphous IZO TFTs.[20,24]

Fig. 10(a) displays the clear saturation of the drain current, I_D, of the reference IZO-channel TFTs by sweeping the drain voltage, V_D, from 0 V to 20 V across a range of gate biases, V_G, from −4 V to 10 V (2 V steps). At a fixed saturated drain voltage (V_D = 20 V), IZO-TFT transfer characteristics were obtained as shown in Fig. 10(b) by scanning V_G from −10 V to 20 V. The on/off ratio, saturation field effect mobility (μ_{sat}), and threshold voltage (V_T) were then estimated using the following equation, which relates the drain current to μ_{sat}, V_G, V_T, oxide capacitance (C_{ox} = 6.903 × 10^{-8} F cm^{-2} for 50 nm SiO_2), and the device aspect ratio of channel width (W) to length (L), W/L = 1200/60 μm/μm:

$$I_D = \mu_{sat} C_{ox} \frac{W}{2L} (V_G - V_T)^2 \quad (6)$$

The resulting on/off ratios of the reference IZO-based TFTs are shown to be $>10^7$, estimated *via* the minimum ($\sim 10^{-10}$ A) and maximum ($\sim 10^3$ A) drain currents, exceeding the required on/off ratio for active matrix display applications of 10^6. Saturation field effect mobility values reached values as high as 21.92 cm^2 V^{-1} s^{-1},

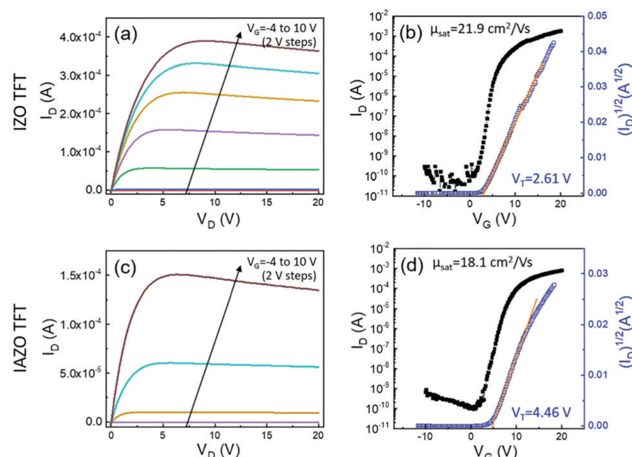

Fig. 10 Output and transfer characteristics of (a and b) IZO-channel and (c and d) IAZO-channel TFTs, which exhibit desirable drain current saturation behaviors, high on/off ratios ($>10^7$), and high saturation field effect mobilities (>18 cm^2 V^{-1} s^{-1}).

 This journal is © The Royal Society of Chemistry 2020

similar to previously reported values for IZO-based TFTs.[20,24] After the extrapolation of the linear regime of the $(I_D)^{1/2}$ *vs.* V_G plot to the *x*-axis (where $I_D = 0$), the threshold voltage is determined to be approximately 2.61 V.

Fig. 10(c) and (d) show the output and transfer characteristics of IAZO-channel TFTs, respectively. IAZO-channel TFTs were fabricated utilizing the same manufacturing parameters as the IZO-based TFTs, with the exception of Al incorporation into the channel layer material *via* co-sputtering of IZO and Al targets. In the output characteristics visualized in Fig. 10(c), clear drain current saturation can be observed at the measured drain and gate biases with no indication of current crowding, particularly in the low drain bias regime, suggesting ohmic contact at the channel/metallization interface. The drain current of IAZO TFTs at the maximum gate bias observed (10 V) is slightly less than that of the IZO-based TFTs, but the overall magnitude is comparable to each other. An increase in I_D is observed at gate biases >2 V for binary IZO-based TFTs, while the increase for ternary IAZO-based devices is shown at $V_G > 4$ V. This variance may be explained further by the differences seen in the measured threshold voltages. The threshold voltage of IAZO TFTs is found to be $\sim$4.46 V, extrapolated from the transfer performance shown in Fig. 10(d). The threshold voltage of a field effect transistor is defined as the minimum gate-to-source voltage to drive a high enough conducting path (*i.e.*, channel) between the source and drain metallization and, therefore, IAZO TFTs require slightly higher V_G to modulate the channel and I_D at $V_G > \sim V_T$. Further details regarding V_T will follow later to discuss channel carrier density, trap density at the channel/dielectric interface, and the magnitude of V_T.

The saturation field effect mobility of IAZO TFTs is shown to be $\sim$18.13 $cm^2\ V^{-1}\ s^{-1}$, which is comparable to the binary cation channel IZO TFTs and yields considerably higher mobility compared to other ternary cation channel TFTs, such as IGZO ($\sim$2–10 $cm^2\ V^{-1}\ s^{-1}$),[67,68] InSiZnO ($\sim$1–7 $cm^2\ V^{-1}\ s^{-1}$),[34] and IZnSnO ($\sim$1–5 $cm^2\ V^{-1}\ s^{-1}$).[76] The high field effect mobility of IAZO-based TFTs suggests strong potential for application in next generation TFT technologies and display applications. It should be noted that TFT field effect mobilities are generally lower than Hall effect mobilities due to the increase in surface scattering associated with a decrease in the channel thickness, as well as the carrier density-dependent charge screening phenomena observed in In_2O_3-based amorphous oxides as shown in this study and other reports.[1,77]

While obtaining direct measurements of channel carrier density (n_{ch}) through the Hall Effect method has proven difficult for AOS channel layers (due to their resistive nature), the difference between the two channel carrier densities ($\Delta n_{ch} = n_{ch,IZO} - n_{ch,IAZO}$) can be determined from the considerations of threshold voltage and interfacial trap density. The threshold voltage is determined using[73]

$$V_T = \frac{q(Q_i + Q_d)}{C_{ox}} + \phi_{ms} + \phi_F \quad (7)$$

where Q_i is the effective trap density at the channel/dielectric interface, Q_d is the depletion charge estimated using $Q_d = n_{ch} \times l_d$ where the maximum depletion depth, l_d, is approximated by the channel thickness (30 nm), Φ_{ms} is the work function difference between the gate (Φ_m) and channel (Φ_s), and Φ_F is the difference between the Fermi level (E_F) and the intrinsic level (E_i) for the n-type semiconductor (*i.e.*, E_F–E_i). While both Φ_{ms} and Φ_F are functions of channel carrier density, the change in the sum of the two, $\Delta(\phi_{ms} + \phi_F)$, is approximated by the change in the Fermi level, ΔE_F, which, in this case, is negligible ($\ll$1 eV). The threshold voltage difference may then be simplified to

$$\Delta V_T = \frac{q\Delta(Q_i + Q_d)}{C_{ox}} \quad (8)$$

where the interfacial trap density, Q_i, is estimated from the sub-threshold swing (S.S.) using

$$Q_i = \left(\frac{q(\text{S.S.})\log(e)}{kT} - 1\right)\frac{C_{ox}}{q} \quad (9)$$

and

$$\text{S.S.} = \frac{dV_G}{d(\log\ I_D)} \quad (10)$$

Through the inverse slopes of Fig. 10(b) and (d), the sub-threshold swings, S.S. were determined to be $\sim$0.68 V $decade^{-1}$ and $\sim$0.96 V $decade^{-1}$ for IZO and IAZO TFTs, respectively. From the calculated values of V_T and S.S. the interfacial trap densities of each device were discovered. These values, as well as previously discussed parameters, are summarized in Table 1. Using eqn (8) in combination with the parameter values in Table 1, the Δn_{ch} of the two devices reveals that the IAZO-based channel carrier density is less than that of the IZO-based TFTs by $\sim 4.14 \times 10^{17}\ cm^{-3}$, further demonstrating the carrier suppression effects of Al incorporation into the channel layer.

While identical sputtering conditions were used for both IZO-based and IAZO-based TFTs to eliminate any uncertainty arising from process parameter variation, the measured V_T values for IAZO-channel TFTs are relatively high. However, the threshold voltage of IAZO TFTs can be further engineered by tuning the oxygen content in the sputter gas to control carrier density, by enhancing the quality of the SiO_2 gate dielectric layer, by applying high-*k* dielectric materials with thinner layers with respect to dielectric capacitance, or through further fine matching of the work function between the channel and metallization layers.

There have been several efforts to explore a similar oxide system incorporating the three cations of In, Al and Zn. Cho *et al.*,[78] reported on the anode application in organic solar cells of roll-to-roll sputtered IAZO (5 wt% Al_2O_3), exhibiting a resistivity of $\sim 2.1 \times 10^{-3}\ \Omega$ cm, similar to that of 8.9 wt% IAZO

Table 1 Properties of amorphous IZO and IAZO TFTs

	On/off ratio	μ_{sat} [$cm^2\ V^{-1}\ s^{-1}$]	S [V $decade^{-1}$]	V_{Th} [V]	Q_i [cm^2]
IZO TFTs	$>10^7$	21.92	0.68	2.61	4.53×10^{12}
IAZO TFTs	$>10^7$	18.13	0.96	4.46	6.57×10^{12}

in the present study, as well as enhanced mechanical stability. However, the majority of other reports in the literature focus on Zn (or ZnO)-rich IAZO films, which require a series of post-process annealing processes at 250–500 °C to obtain functioning TFTs. The present study focuses on In_2O_3-rich IAZO (90 wt% In_2O_3)[70,79] and its fabrication for TFT applications at room temperature (without annealing). Although direct assessments between materials with different matrices and doping amounts are not available, it is worth comparing properties and device performance. Park *et al.*,[80] grew Zn-rich IAZO films through a solution process with 5 mol% Al in the In/Zn solution with a 30/70 atomic ratio (no final Al or other cation concentrations were investigated in this study) and used a series of annealing processes, which consisted of air annealing at 400 °C for an hour, followed by vacuum annealing at temperatures up to ~300 °C after purging the chamber with N_2. Top-gated TFTs were fabricated; however, the saturation field effect mobility was as low as ~0.66 $cm^2\ V^{-1}\ s^{-1}$, showing little potential for future application. Bak *et al.*, sputter-deposited ZnO-rich IAZO films (no cation concentrations reported) by adding In_2O_3 into AlZnO (2 wt% Al) to investigate the sputter power effect on the ZnO-rich IAZO TFT performance. After a set of annealing processes at 200 °C in vacuum and 250 °C in air, the field effect mobilities were shown to vary as a function of sputter power from ~0.7 $cm^2\ V^{-1}\ s^{-1}$ to ~25 $cm^2\ V^{-1}\ s^{-1}$. Yue *et al.*[81] used solution-processed Zn-rich IAZO (an In/Zn atomic ratio of 50/50) as the channel in TFTs, using 500 °C annealing in air for two hours and obtained the maximum field effect mobility of ~25 $cm^2\ V^{-1}\ s^{-1}$ in the linear regime. Some of the field effect mobilities of Zn-rich IAZO TFTs achieved after annealing at high temperatures up to 500 °C in the literature are slightly higher or comparable to those of the un-annealed TFTs demonstrated in this report. In general, low-thermal budget processing (*e.g.*, no anneal) is highly favorable in next generation device applications such as potential flexible and foldable displays that require the use of heat-sensitive polymer or paper substrates.

Overall, the reported material system of IAZO demonstrates the noteworthy enhancement of amorphous phase stability; the preservation of a high carrier mobility in spite of the addition of the third cation species of Al; the ability to suppress the carrier generation for TFT channel application; and a high TFT field effect mobility. All these properties of IAZO are expected to contribute to high performance electronic and optoelectronic devices such as next generation transparent displays with enhanced sustainability and reliability.

Conclusions

The effect of Al incorporation into the binary standard AOS material (IZO) was systematically investigated: (i) the amorphous phase stability was significantly enhanced by the addition of Al. Unlike IZO, the amorphous phase of which was transformed to the poly-crystalline bixbyite IZO at an annealing temperature of 500 °C, no significant phase changes were observed at Al concentrations higher than 4 wt%; (ii) unlike other third cation species such as Ga, Si and Hf, the carrier mobilities of which are as low as 3–10 $cm^2\ V^{-1}\ s^{-1}$, a considerably high carrier mobility (Hall effect) of 25–45 $cm^2\ V^{-1}\ s^{-1}$ remained before and after annealing in air at up to 550 °C in this study; and (iii) the ability to suppress the carrier generation was clearly demonstrated due to a higher binding energy between Al and O, compared to In–O and Zn–O. Proof-of-concept IAZO-based TFTs demonstrate high field effect mobilities (18–20 $cm^2\ V^{-1}\ s^{-1}$), which are comparable to those of binary cation IZO TFTs. For TFT devices, which are essential components as pixel driving elements in displays, the achievements of greater thermal phase stability, preservation of a high carrier mobility after using additional cations, and carrier suppression are highly expected to advance the AOS materials and their applications in devices that require high performance such as a fast switching speed and reliable device performance during service.

Conflicts of interest

There are no conflicts to declare.

Acknowledgements

The authors gratefully acknowledge the financial support of the U.S. National Science Foundation (NSF; Award No. ECCS-1931088). SL acknowledges the support from Purdue University, the Purdue Research Foundation (Grant No. 60000029) and the Polytechnic RDE SEED program. KN is supported by the Basic Science Research Program (NRF-2018R1A2B600219413) through the NRF Korea funded by the Ministry of Science and ICT. HWS acknowledges the support from the Improvement of Measurement Standards and Technology for Mechanical Metrology (Grant No. 20011028) by KRISS.

Notes and references

1 S. Lee and D. C. Paine, *Appl. Phys. Lett.*, 2013, **102**, 052101.
2 K. Nomura, H. Ohta, A. Takagi, T. Kamiya, M. Hirano and H. Hosono, *Nature*, 2004, **432**, 488–492.
3 S. Lee and D. C. Paine, *Appl. Phys. Lett.*, 2014, **104**, 252103.
4 E. Fortunato, D. Ginley, H. Hosono and D. C. Paine, *MRS Bull.*, 2007, **32**, 242–247.
5 A. Maho, S. Nicolay, L. Manceriu, G. Spronck, C. Henrist, R. Cloots, B. Vertruyen and P. Colson, *J. Electrochem. Soc.*, 2017, **164**, H25–H31.
6 A. Venkatanarayanan and E. Spain, in *Comprehensive Materials Processing*, ed. S. Hashmi, G. F. Batalha, C. J. Van Tyne and B. Yilbas, Elsevier, Oxford, 2014, pp. 47–101, DOI: 10.1016/B978-0-08-096532-1.01303-0.
7 S. Zhao, D. Choi, T. Lee, A. K. Boyd, P. Barbara, E. Van Keuren and J.-i. Hahm, *J. Phys. Chem. C*, 2015, **119**, 14483–14489.
8 B. G. Lewis and D. C. Paine, *MRS Bull.*, 2000, **25**, 22–27.

This journal is © The Royal Society of Chemistry 2020

9 T. J. Coutts, D. L. Young and X. Li, *MRS Bull.*, 2000, **25**, 58–65.
10 C. W. Ow-Yang, D. Spinner, Y. Shigesato and D. C. Paine, *J. Appl. Phys.*, 1998, **83**, 145–154.
11 S. Lee, S.-H. Kim, Y. Kim, A. I. Kingon, D. C. Paine and K. No, *Mater. Lett.*, 2012, **85**, 88–90.
12 R. G. Gordon, *MRS Bull.*, 2000, **25**, 52–57.
13 A. S. Reed, D. C. Paine and S. Lee, *J. Electron. Mater.*, 2016, **45**, 6310–6316.
14 J.-S. Park, J. K. Jeong, Y.-G. Mo, H. D. Kim and C.-J. Kim, *Appl. Phys. Lett.*, 2008, **93**, 033513.
15 C. Wei Shih, A. Chin, C. Fu Lu and W. Fang Su, *Sci. Rep.*, 2016, **6**, 19023.
16 E. N. Dattoli, Q. Wan, W. Guo, Y. Chen, X. Pan and W. Lu, *Nano Lett.*, 2007, **7**, 2463–2469.
17 J. Xu, M. Wen, X. Zhao, L. Liu, X. Song, P.-T. Lai and W.-M. Tang, *Nanotechnology*, 2018, **29**, 345201.
18 Y.-Q. Yang, Y. Duan, P. Chen, F.-B. Sun, Y.-H. Duan, X. Wang and D. Yang, *J. Phys. Chem. C*, 2013, **117**, 20308–20312.
19 P. Barquinha, A. Pimentel, A. Marques, L. Pereira, R. Martins and E. Fortunato, *J. Non-Cryst. Solids*, 2006, **352**, 1749–1752.
20 D. C. Paine, B. Yaglioglu, Z. Beiley and S. Lee, *Thin Solid Films*, 2008, **516**, 5894–5898.
21 S. Lee and D. C. Paine, *Appl. Phys. Lett.*, 2011, **98**, 262108.
22 K. Nomura, T. Kamiya, M. Hirano and H. Hosono, *Appl. Phys. Lett.*, 2009, **95**, 013502.
23 Y. Tai, H. Liu, P. Chan and S. Chiu, *IEEE Electron Device Lett.*, 2018, **39**, 696–698.
24 S. Lee, H. Park and D. C. Paine, *J. Appl. Phys.*, 2011, **109**, 063702.
25 T. H. Meen, S. Prior and A. Lam, *Innovation in Design, Communication and Engineering: Proceedings of the 2014 3rd International Conference on Innovation, Communication and Engineering (ICICE 2014), Guiyang, Guizhou, P.R. China, October 17–22*, 2014, CRC Press, 2015.
26 D. C. Paine, T. Whitson, D. Janiac, R. Beresford, C. O. Yang and B. Lewis, *J. Appl. Phys.*, 1999, **85**, 8445–8450.
27 S. Lee, K. Park and D. C. Paine, *J. Mater. Res.*, 2012, **27**, 2299–2308.
28 J. J. Jia, N. Oka and Y. Shigesato, *J. Appl. Phys.*, 2013, **113**, 163702.
29 S. Lee, Y. Song, H. Park, A. Zaslavsky and D. C. Paine, *Solid-State Electron.*, 2017, **135**, 94–99.
30 A. Takagi, K. Nomura, H. Ohta, H. Yanagi, T. Kamiya, M. Hirano and H. Hosono, *Thin Solid Films*, 2005, **486**, 38–41.
31 Y. Kikuchi, K. Nomura, H. Yanagi, T. Kamiya, M. Hirano and H. Hosono, *Thin Solid Films*, 2010, **518**, 3017–3021.
32 W. H. Jeong, G. H. Kim, H. S. Shin, B. Du Ahn, H. J. Kim, M.-K. Ryu, K.-B. Park, J.-B. Seon and S. Y. Lee, *Appl. Phys. Lett.*, 2010, **96**, 093503.
33 E. Chong, K. C. Jo and S. Y. Lee, *Appl. Phys. Lett.*, 2010, **96**, 152102.
34 E. Chong, S. H. Kim and S. Y. Lee, *Appl. Phys. Lett.*, 2010, **97**, 252112.
35 W. S. Choi, H. Jo, M. S. Kwon and B. J. Jung, *Curr. Appl. Phys.*, 2014, **14**, 1831–1836.
36 B. Yaglioglu, H. Y. Yeom and D. C. Paine, *Appl. Phys. Lett.*, 2005, **86**, 261908.
37 T. L. Cottrell, *The Strengths of Chemical Bonds*, Butterworth, 1961.
38 B. B. Darwent, *Bond Dissociation Energies in Simple Molecules*, U.S. National Bureau of Standards, 1970.
39 S. W. Benson, *J. Chem. Educ.*, 1965, **42**, 502.
40 J. A. Kerr, *Chem. Rev.*, 1966, **66**, 465–500.
41 K. Nomura, A. Takagi, T. Kamiya, H. Ohta, M. Hirano and H. Hosono, *Jpn. J. Appl. Phys.*, 2006, **45**, 4303–4308.
42 E. Chong, Y. S. Chun and S. Y. Lee, *Appl. Phys. Lett.*, 2010, **97**, 102102.
43 J.-S. Seo, J.-H. Jeon, Y. H. Hwang, H. Park, M. Ryu, S.-H. K. Park and B.-S. Bae, *Sci. Rep.*, 2013, **3**, 2085.
44 P. Agoston, K. Albe, R. M. Nieminen and M. J. Puska, *Phys. Rev. Lett.*, 2009, **103**, 245501.
45 P. Agoston and K. Albe, *Phys. Rev. B: Condens. Matter Mater. Phys.*, 2010, **81**, 195205.
46 P. Reunchan, X. Zhou, S. Limpijumnong, A. Janotti and C. G. Van de Walle, *Curr. Appl. Phys.*, 2011, **11**, S296–S300.
47 J. H. W. De Wit, G. Van Unen and M. Lahey, *J. Phys. Chem. Solids*, 1977, **38**, 819–824.
48 N. E. Sosa, C. Chen, J. Liu, S. Xie, T. J. Marks and M. C. Hersam, *J. Am. Chem. Soc.*, 2010, **132**, 7347–7354.
49 G. Frank and H. Köstlin, *Appl. Phys. A: Solids Surf.*, 1982, **27**, 197–206.
50 M. Kaveh and N. Wiser, *Adv. Phys.*, 1984, **33**, 257–372.
51 S. Lee, B. Bierig and D. C. Paine, *Thin Solid Films*, 2012, **520**, 3764–3768.
52 H. Hosono, *Thin Solid Films*, 2007, **515**, 6000–6014.
53 H. Hosono, in *Handbook of Visual Display Technology*, ed. J. Chen, W. Cranton and M. Fihn, Springer Berlin Heidelberg, Berlin, Heidelberg, 2012, pp. 729–749, DOI: 10.1007/978-3-540-79567-4_52.
54 H. Nakazawa, Y. Ito, E. Matsumoto, K. Adachi, N. Aoki and Y. Ochiai, *J. Appl. Phys.*, 2006, **100**, 093706.
55 C. W. Ow-Yang, H.-y. Yeom and D. C. Paine, *Thin Solid Films*, 2008, **516**, 3105–3111.
56 Y. Shigesato, D. C. Paine and T. E. Haynes, *Jpn. J. Appl. Phys., Part 2*, 1993, **32**, L1352–L1355.
57 M. R. Abidian and D. C. Martin, *Biomaterials*, 2008, **29**, 1273–1283.
58 D. K. Taggart, Y. Yang, S.-C. Kung, T. M. McIntire and R. M. Penner, *Nano Lett.*, 2011, **11**, 125–131.
59 J. Tauc, in *Optical Properties of Solids: Papers from the NATO Advanced Study Institute on Optical Properties of Solids Held August 7–20, 1966, at Freiburg, Germany*, ed. S. Nudelman and S. S. Mitra, Springer US, Boston, MA, 1969, pp. 123–136, DOI: 10.1007/978-1-4757-1123-3_5.
60 S. R. Sarath Kumar and S. Kasiviswanathan, *Semicond. Sci. Technol.*, 2009, **24**, 025028.
61 C. Xirouchaki, K. Moschovis, E. Chatzitheodoridis, G. Kiriakidis, H. Boye and P. Morgen, *J. Electron. Mater.*, 1999, **28**, 26–34.
62 Y. Gassenbauer and A. Klein, *Solid State Ionics*, 2004, **173**, 141–145.
63 Y. Ohhata, F. Shinoki and S. Yoshida, *Thin Solid Films*, 1979, **59**, 255–261.

This journal is © The Royal Society of Chemistry 2020

64 G. Gonçalves, E. Elangovan, P. Barquinha, L. Pereira, R. Martins and E. Fortunato, *Thin Solid Films*, 2007, **515**, 8562–8566.

65 T. Minami, *MRS Bull.*, 2000, **25**, 38–44.

66 A. Wang, J. Dai, J. Cheng, M. P. Chudzik, T. J. Marks, R. P. H. Chang and C. R. Kannewurf, *Appl. Phys. Lett.*, 1998, **73**, 327–329.

67 T. Kamiya, K. Nomura and H. Hosono, *Sci. Technol. Adv. Mater.*, 2010, **11**, 044305.

68 T. Kamiya, K. Nomura and H. Hosono, *Phys. Status Solidi A*, 2009, **206**, 860–867.

69 G. Drewelow, A. Reed, C. Stone, K. Roh, Z.-T. Jiang, L. N. T. Truc, K. No, H. Park and S. Lee, *Appl. Surf. Sci.*, 2019, **484**, 990–998.

70 B. Yaglioglu, Y. J. Huang, H. Y. Yeom and D. C. Paine, *Thin Solid Films*, 2006, **496**, 89–94.

71 T. Moriga, D. D. Edwards, T. O. Mason, G. B. Palmer, K. R. Poeppelmeier, J. L. Schindler, C. R. Kannewurf and I. Nakabayashi, *J. Am. Ceram. Soc.*, 1998, **81**, 1310–1316.

72 Y. S. Jung, H. Y. Seo, D. W. Lee and D. Y. Jeon, *Thin Solid Films*, 2003, **445**, 63–71.

73 B. G. Streetman and S. K. Banerjee, *Solid State Electronic Devices*, Pearson Prentice Hall, 6th edn, 2006.

74 Y.-L. Wang, F. Ren, W. Lim, D. P. Norton, S. J. Pearton, I. I. Kravchenko and J. M. Zavada, *Appl. Phys. Lett.*, 2007, **90**, 232103.

75 K. Nomura, A. Takagi, T. Kamiya, H. Ohta, M. Hirano and H. Hosono, *Jpn. J. Appl. Phys., Part 1*, 2006, **45**, 4303–4308.

76 Q. Jiang, J. Lu, J. Cheng, X. Li, R. Sun, L. Feng, W. Dai, W. Yan and Z. Ye, *Appl. Phys. Lett.*, 2014, **105**, 132105.

77 A. J. Leenheer, J. D. Perkins, M. F. A. M. van Hest, J. J. Berry, R. P. O'Hayre and D. S. Ginley, *Phys. Rev. B: Condens. Matter Mater. Phys.*, 2008, **77**, 115215.

78 D.-Y. Cho, K.-H. Kim, T.-W. Kim, Y.-J. Noh, S.-I. Na, K.-B. Chung and H.-K. Kim, *Org. Electron.*, 2015, **24**, 227–233.

79 B. Yaglioglu, H. Y. Yeom, R. Beresford and D. C. Paine, *Appl. Phys. Lett.*, 2006, **89**, 062103.

80 M. J. Park, J. Y. Bak, J. S. Choi and S. M. Yoon, *ECS Solid State Lett.*, 2014, **3**, Q44–Q46.

81 L. Yue, H. Pu, H. Li, S. Pang and Q. Zhang, *J. Phys. D: Appl. Phys.*, 2013, **46**, 445106.

 This journal is © The Royal Society of Chemistry 2020